ADVANCED OPTICAL MATERIALS
www.advopticalmat.de

Highly Sensitive Broadband Bolometric Photodetectors based on 2D $PdSe_2$ Thin Film

Rui Zhang, Zhuojun Yang, Liwen Liu, Jie Lin, Shaofeng Wen, You Meng, Yi Yin, Changyong Lan, Chun Li,* Yong Liu, and Johnny C. Ho**

$PdSe_2$, a semiconductor with a narrow band gap, shows tremendous promise for high-performance broadband photodetectors. In this study, highly sensitive, broadband, and flexible $PdSe_2$ thin film photodetectors on polyimide (PI) substrates that can detect light from the UV (365 nm) to infrared (2200 nm) regions are reported. The devices with thick (21 nm) $PdSe_2$ films show decent performance with a decent responsivity of 37.6 mA W^{-1} at 1550 nm and a fast response time. For the thick $PdSe_2$ film, the bolometric effect dominates the positive photoresponse across all wavelength regions, whereas for the thin $PdSe_2$ film (4.5–13 nm), which shows both positive and negative photoresponses, it dominates in the infrared region. The negative photoresponse of thin $PdSe_2$ in the UV to the VIS region is attributed to the charge transfer-related adsorption-desorption of gas molecules. Detailed investigations revealed that the temperature coefficient of resistance (TCR) value is closely correlated to film thickness, with the thinnest film exhibiting the highest absolute TCR value of up to 4.3% $°C^{-1}$. The value is much larger than that of metals, most 2D materials, amorphous Si, and even commercial VO_x. These findings suggest that $PdSe_2$ films have a promising future in broadband photodetectors.

1. Introduction

Photodetectors are devices capable of converting light signals to electric signals, and they have numerous applications. A broadband photodetector is particularly in high demand for compact, intelligent imaging and sensing systems.[1–3] However, realizing broadband photodetection is challenging. For instance, the most commonly used imaging sensor is CCD, which is made from Si and cannot detect light with wavelengths exceeding 1100 nm. Although other semiconducting materials with narrow bandgaps, such as InGaAs and HgCdTe, are also used to fabricate photodetectors with broadband response, these technologies are complex and costly. Therefore, new materials with novel optoelectronic properties are highly desired for broadband photodetectors.

Photodetectors based on 2D materials have been extensively explored In the past few decades due to their exotic optoelectronic properties.[4,5] The most studied material is graphene, which has universal light absorption across a wide range of wavelengths. However, the low absorptivity of graphene often leads to poor responsivity, constraining its wide applications in photodetectors.[6] Semiconducting 2D materials with high light absorptivity, such as transition metal dichalcogenides (TMD),[7,8] black phosphorene (BP),[9,10] and Bi_2O_2Se,[11,12] etc., are encouraging for high-performance photodetectors. Nevertheless, the band gaps of most TMDs are large, and photodetectors made from TMD can only work in the VIS or near-infrared (NIR) band range. Even though BP has a narrow band gap (0.3 – 2.0 eV), its ambient instability limits its applications. Due to their strong layer-dependent band gaps and long-term material stability, noble metal dichalcogenides, such as $PtSe_2$,[13–15] $PtTe_2$,[16,17] $PdSe_2$,[18–24] and their heterojunctions have been attracting considerable attention for broadband photodetection in recent years. Particularly, $PdSe_2$ shows a thickness-dependent bandgap from 0.03 to 1.37 eV,[25,26] ensuring broadband photon absorption and detection. Based on an exfoliated single-crystalline $PdSe_2$ flake, an ultra-broadband photodetector from the VIS to terahertz (THz) region driven by a multiphysical mechanism was realized.[27] The $PdSe_2$ heterojunctions ($PdSe_2/MoS_2$, $PdSe_2$/germanium nanocone, etc.)[25,28–35] also exhibit high responsivity and broadband photodetection (even from VIS to 10.6 μm). Until now, the mechanisms of broadband photodetectors based on $PdSe_2$ include photoconductivity (PC) effect, photovoltaic (PV) effect, and photothermoelectric (PTE) effect. As a semiconductor with a narrow band gap, the carrier concentration

R. Zhang, Z. Yang, L. Liu, J. Lin, S. Wen, Y. Yin, C. Lan, C. Li, Y. Liu
State Key Laboratory of Electronic Thin Films and Integrated Devices
School of Optoelectronic Science and Engineering
University of Electronic Science and Technology of China
Chengdu611731, P. R. China
E-mail: cylan@uestc.edu.cn; lichun@uestc.edu.cn
Y. Meng, J. C. Ho
Department of Materials Science and Engineering
City University of Hong Kong
Hong Kong999077, P. R. China
E-mail: johnnyho@cityu.edu.hk
J. C. Ho
Institute for Materials Chemistry and Engineering
Kyushu University
Fukuoka816–8580, Japan

The ORCID identification number(s) for the author(s) of this article can be found under https://doi.org/10.1002/adom.202301055

DOI: 10.1002/adom.202301055

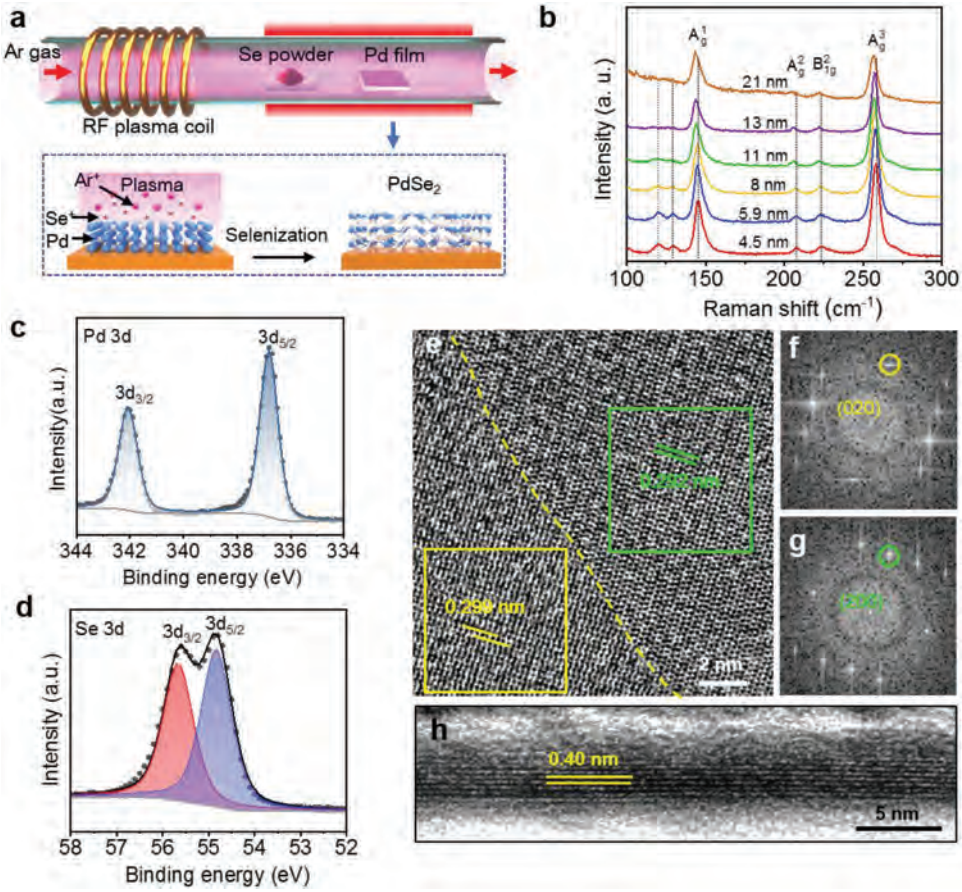

Figure 1. Growth setup and structural characterization of the $PdSe_2$ films. a) Schematic of the growth setup and the selenization process. b) Raman spectra of the $PdSe_2$ films with different thicknesses prepared at 200 °C. c) XPS spectrum of Pd 3d. d) XPS spectrum of Se 3d. e) HRTEM image of the $PdSe_2$ film. f) and g) the corresponding FFT of the marked areas in (e). h) Cross-section HRTEM image of the $PdSe_2$ film. The thickness of samples shown in (c) to (h) is 4.5 nm.

of the material should be sensitive to temperature due to the substantial contribution from thermally excited electron-hole pairs. Utilizing the temperature-sensitive resistance, called the bolometric effect, a broadband photodetector can be realized. To the best of our knowledge, however, the bolometric effect for $PdSe_2$ is rarely explored.

In this work, we report broadband photodetectors fabricated from ultrathin $PdSe_2$ films prepared by plasma-enhanced metal-selenization. The bolometric effect and negative photoconductivity (NPC) effect was found to coexist in $PdSe_2$ films photodetectors. For the thinner $PdSe_2$ films (4.5–13 nm) photodetectors, the NPC effect is the dominant detection mechanism in the UV region (365 nm) to VIS (532 nm) region, the bolometric effect becomes dominant in the near-infrared region from 808 nm to 2200 nm. Only a bolometric effect was observed in the thicker $PdSe_2$ films (21 nm) photodetectors which show a wide range of responses from the UV region (365 nm) to the near-infrared region (2200 nm). A maximum responsivity of 37.5 mA W^{-1} was achieved at 1500 nm with a decent response speed. The absolute value of the temperature coefficient of resistance (TCR) increases with the decrease in film thickness. A TCR value up to 4.3% $°C^{-1}$ was achieved, which is higher than that of most metals, amorphous Si, and even commercial VO_x, suggesting promising applications in broadband photodetectors. Owing to its high sensitivity, infrared images can be captured using a 4×4 photodetector array. Our work suggests that large-area $PdSe_2$ film has a remarkable bolometric effect and shows promising potential for broadband photodetection.

2. Results and Discussion

The $PdSe_2$ films were synthesized by plasma-enhanced metal-selenization. A schematic of the setup is shown in **Figure 1**a. Pd films were deposited on PI substrates or SiO_2/Si substrates. Then the Pd films were converted into $PdSe_2$ films in a low-pressure CVD system. Using inductive plasma, we can obtain the $PdSe_2$ films at a low temperature (200 °C). The bombardment of Ar plasma can ionize selenium (Se) powder into Se radicals with enhanced chemical reactivity, which can then interact with Pd atoms, despite the fact that selenium powder is difficult to evaporate at 200 °C. As confirmed by Raman spectra of the $PdSe_2$ films (Figure 1b), the Pd films with different thicknesses can be completely converted into $PdSe_2$ films. The Raman spectra of the films exhibit four distinct peaks at ≈145, 208, 223, and 258 cm^{-1} corresponding to the A_g^1, A_g^2, B_{1g}^2, and A_g^3 modes of the orthorhombic $PdSe_2$ lattice, respectively.[36] The

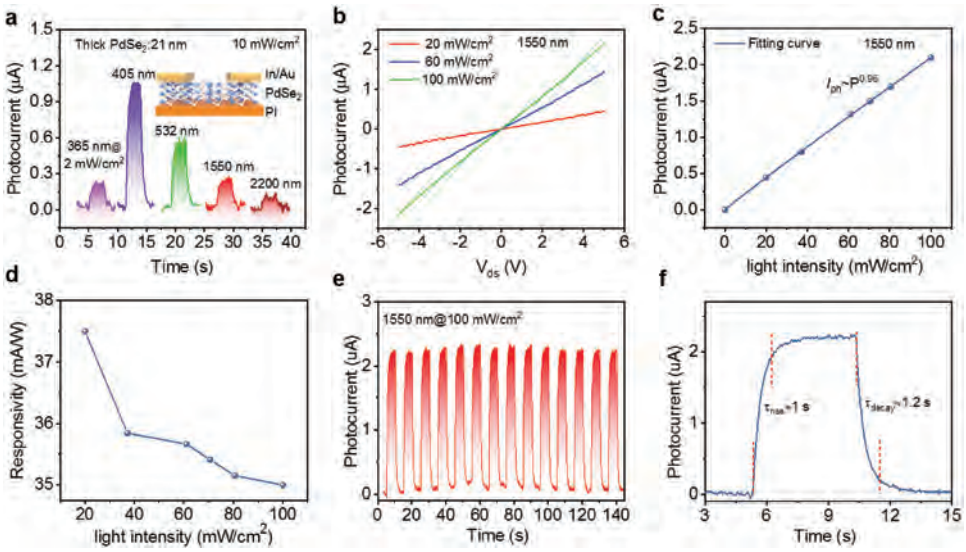

Figure 2. Photodetection performance of a thick $PdSe_2$ film (21 nm) photodetector. a) Photocurrent verse time under the illumination of light with different wavelengths. Inset: schematic of the $PdSe_2$ device on a PI substrate. b) Photocurrent verse applied voltage under the light illumination (1550 nm) with different light intensities. c) Photocurrent verse light intensity. d) Responsivity verse light intensity. e) Photocurrent as a function of time under a 1550 nm laser with a light intensity of 100 mW cm^{-2}. f) The response speed of the device in the single-period response curves shown in (e). The applied voltage and light wavelength for (c) to (f) are 5 V and 1550 nm, respectively.

corresponding AFM thickness measurement was shown in Figure S1 (Supporting Information). To further check whether the Pd film is fully converted into $PdSe_2$ or not, X-ray photoelectron spectroscopy (XPS) spectra of the film were measured. Figure 1c,d shows the peaks of Pd 3d and Se 3d, where the Pd $3d_{3/2}$ and $3d_{5/2}$ peaks are located at 342.2 and 336.9 eV, and the Se $3d_{3/2}$ and $3d_{5/2}$ peaks are located at 55.8 and 54.9 eV, respectively. The peak positions are consistent with the CVD-grown $PdSe_2$ single-crystal nanosheets and polycrystalline $PdSe_2$ films.[37,38] From the peak area analysis, the atomic ratio of Pd and Se is calculated to be ≈1:2, indicating the stoichiometric of the $PdSe_2$ film. To study the microstructures of the $PdSe_2$ films, transmission electron microscopy (TEM) measurements were carried out. Apparent grain boundaries are observed from top-view high-resolution TEM (HRTEM) image (Figure 1e), revealing its polycrystalline nature. Clear lattice fringes can be observed, indicating the well-crystalline structure of the $PdSe_2$ grains. The lattice spacings of the fringes can be measured to be 0.299 and 0.292 nm, corresponding to the (020) and (200) planes of the $PdSe_2$, respectively. The result is well-matched with the fast Fourier transform (FFT) patterns shown in Figure 1f,g. From the cross-sectional HRTEM image, the periodic atomic arrangement of $PdSe_2$ with an inter-layer spacing of 0.40 nm was observed (Figure 1h), which is consistent with the lattice spacing of (002) planes. The results of above structural characterization suggest the good crystallinity of the films.

As $PdSe_2$ is a semiconductor with a narrow bandgap, intriguing photodetector performance is expected. We fabricated $PdSe_2$ thin film photodetectors both on SiO_2/Si and PI substrates. Interestingly, almost no detectable photoresponse was observed for the device fabricated on SiO_2/Si device. However, considerable photoresponse was observed for devices on the PI substrate (Figure S2, Supporting Information). In addition, the photoresponse differs between thick films (> 13 nm) and thin films (≤ 13 nm). The photoresponse of thick film (21 nm) is discussed first. As shown in **Figure 2**a, the photodetector exhibits broadband spectrum response, ranging from 365 to 2200 nm. To have a more deep understanding of the performance of the photodetector, the photocurrent under infrared light illumination (1550 nm) with different light intensities were measured and are shown in Figure 2b. The photocurrent increases with the applied voltage and light intensity. The photocurrent as a function of light intensity is shown in Figure 2c. The photocurrent almost increases linearly with light intensity. The data can be well fitted by the following equation.

$$I_{ph} = AP^{\alpha} \quad (1)$$

where I_{ph} is the photocurrent, A and α are the fitting parameters. The index α is ≈0.96 according to the fitting, indicating the almost linear relationship between photocurrent and light intensity. The photoresponsivity is estimated from the equation:

$$R = I_{ph}/S \quad (2)$$

where R is the responsivity, S is the photosensitive area. The maximum photoresponsivity can reach 37.6 mA W^{-1} (Figure 2d). To obtain the transient behavior of the photodetector, photocurrent as a function of time under modulated light was measured and the result is shown in Figure 2e. The stable on and off photocurrent suggests the photodetector is very reliable. The response time can be obtained from the single-period response curves of the photocurrent-time curve in Figure 2e. The rise time and decay time are determined to be the time interval for photocurrent rising from 10% to 90% of the stable photocurrent and vice versa, respectively. The rise time is 1 s while the decay time is 1.2 s (Figure 2f), indicating the fast response speed of the photodetector (Table S1, Supporting information). The response

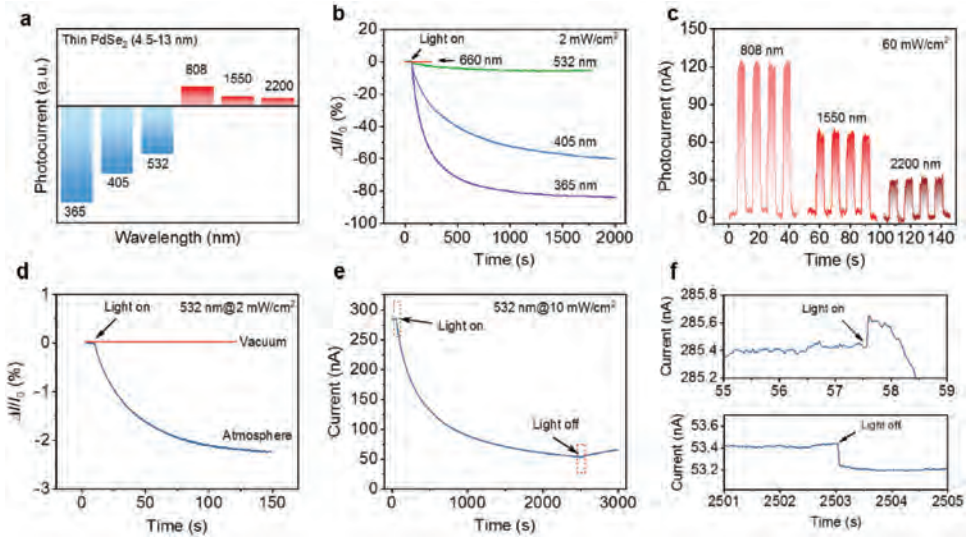

Figure 3. Photodetection performance of thin $PdSe_2$ film-based photodetector. a) Schematic of photocurrent versus light wavelength. b) Photocurrent versus time under light illumination in the near UV–vis region. c) Photocurrent versus time under light illumination in the NIR region. d) Photocurrent versus time for the device in different environments. e) Photocurrent versus time with light on and off in ambient. f) Enlarged parts of the dashed red square regions shown in (e). The applied bias voltage for (b) to (f) is 5 V.

speed of bolometers is dependent on the effectiveness of thermal management.[39] To further enhance the response speed of the device, it may be advantageous to employ a substrate with higher thermal conductivity or implement a bridged device structure.

Generally, the photoresponse mechanism for two-terminal semiconductor devices includes PC, PV, PTE, and bolometric effect.[40] The absence of any response in the device with the same structure on SiO_2/Si suggests that the PC effect may not play a significant role in the device's operation. Although $PdSe_2$ is a semiconductor, the high density of defects in polycrystalline $PdSe_2$ may act as recombination centers for photogenerated carriers, leading to the quench of photocurrent. Therefore, no significant photocurrent was observed on the SiO_2/Si substrates. The drain and source electrodes are of the same metal, and universal light illumination was used during the measurements. Therefore, the PTE effect should not contribute to the photoresponse.[27] Consequently, it is believed that the bolometric effect should be the primary contributor to the photoresponse. The temperature rise for devices on SiO_2/Si should be minimal due to the more significant thermal conductivity and thermal capacity of Si (≈130 W m^{-1} K^{-1} and 700 J Kg^{-1} K^{-1}, respectively)[41] and SiO_2 (≈1.34 W m^{-1} K^{-1} and 725 J Kg^{-1} K^{-1}, respectively).[42] Hence, the resistance increase for $PdSe_2$ on SiO_2/Si is very small, resulting in almost no observable photoresponse. Conversely, the thermal conductivity of PI is significantly smaller (≈0.18 W m^{-1} K^{-1} and 1.95 J Kg^{-1} K^{-1}, respectively),[43] and a considerable temperature change may occur for $PdSe_2$ on PI substrate under light illumination. The distinctive temperature variation of these two types of devices under the same light irradiation was also verified by simulation using the thermal conduction model (Figure S3, Supporting Information).

Interestingly, we found that the thin $PdSe_2$ films also exhibit broadband photoresponse. However, the devices with thin $PdSe_2$ exhibit negative photocurrent when the light wavelength is shorter than 660 nm, as schematically shown in **Figure 3**a. The negative photoresponse effect decreases with increasing wavelength, as shown in Figure 3b. Additionally, the photoresponse is relatively slow, with ≈1500 s required for the photocurrent to stabilize. In contrast, for infrared light illumination, the devices demonstrate a fast response, similar to that of thick $PdSe_2$-based devices (Figure 3c). The negative photoresponse cannot be attributed to the bolometric effect which only leads to an increase in current under light illumination. To determine the exact mechanism, the photoresponse of the devices was measured in different environments. As illustrated in Figure 3d, almost no negative photocurrent is observed for the device measured in a vacuum with pressure of 4.5×10^{-4} Pa. As the gas molecules were significantly reduced, the light-assisted surface-absorption-molecule-induced charge carriers were substantially suppressed compared with the photoresponse observed under atmospheric conditions. Therefore, the negative photocurrent should be attributed to photo-activated gas molecule adsorption/desorption processes.[44,45] In fact, the superimposed positive photocurrent on the negative photoresponse background can still be observed when a very high intensity of light illumination is applied, as shown in Figure 3e,f. The positive photocurrent is likely caused by the bolometric effect, which is supported by detectable temperature elevation upon light illumination (Figure S4, Supporting Information). However, the overall current decreases rapidly in the ambient due to the gas molecule's desorption effect.

According to the results presented above, the photoresponse mechanism for $PdSe_2$ films is proposed. Both bolometric and NPC effects should coexist in the devices. The question arises as to which effect dominates the net photocurrent. The observed phenomena are schematically shown in **Figure 4**a. For thin $PdSe_2$ films, the NPC effect dominates in the UV–vis region, while the bolometric effect dominates in the NIR region. Conversely, for thick $PdSe_2$ films, the bolometric effect is dominant in the measured spectrum region due to the weakening of the surface adsorption effect as the thickness of the film increases.[44] The

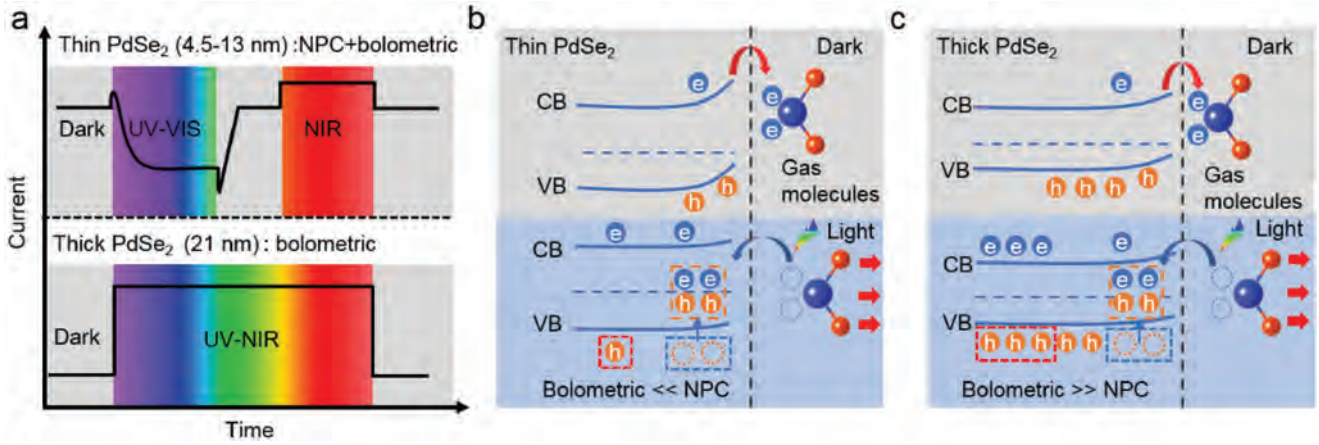

Figure 4. Photoresponse mechanisms. a) Schematic for the photoresponse in different wavelength regions. b) Schematic for the photoresponse mechanism for thin $PdSe_2$ film. c) Schematic for the photoresponse mechanism for thick $PdSe_2$ film.

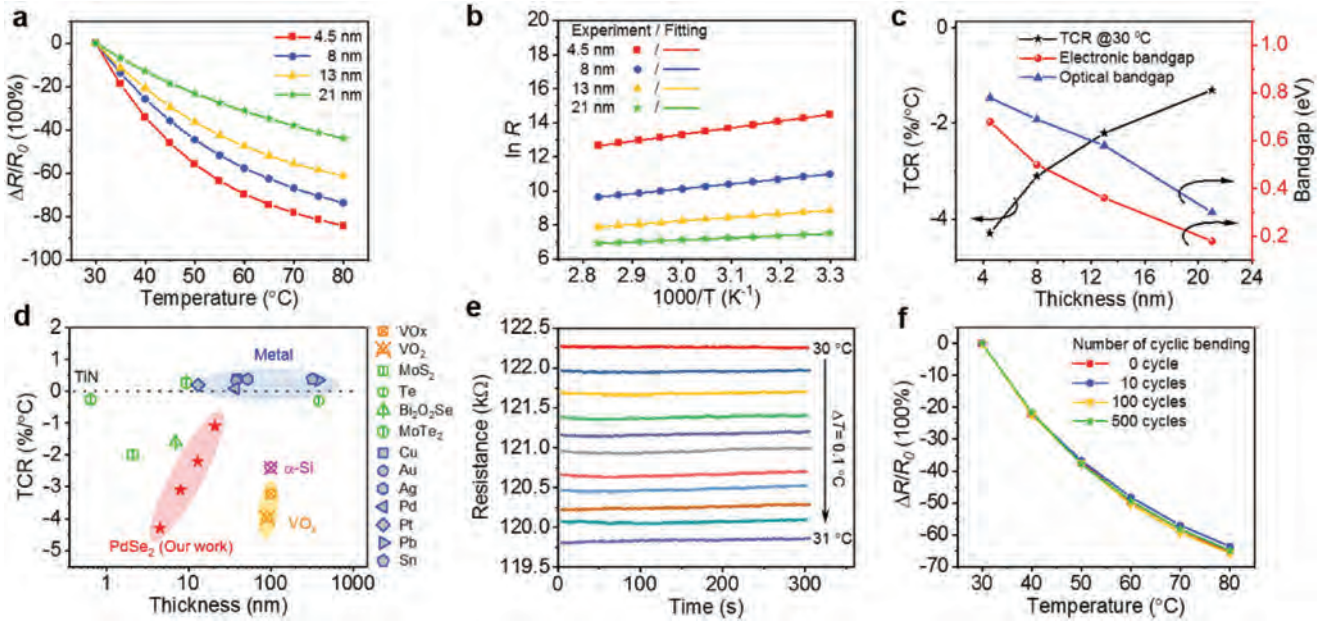

Figure 5. Bolometric effect characterization. a) Relative change of resistance versus temperature for $PdSe_2$ films with different thicknesses. b) ln(R) versus 1000/T plots for $PdSe_2$ films with difference thicknesses. c) TCR, electric bandgap, and optical bandgap as a function of film thickness. d) Collection of TCRs for different materials reported in the literature. e) Resistance versus time at different temperatures. f) Relative change of resistance as a function of temperature with different bending circles.

proposed photoresponse mechanism, as shown schematically in Figure 4b,c, involves the adsorption of gases, such as water and oxygen molecules, which can capture electrons from $PdSe_2$, leading to p-type doping.[45,46] This effect is more pronounced in thin films than that in thick ones. Under light illumination, surface-absorbed gas molecules are removed from the surface, and then free electrons recombine with holes resulting in a decrease in the channel conductivity and the generation of negative photocurrent. Although light absorption can also increase the channel temperature, the bolometric effect is much weaker than the NPC effect, resulting in only a negative photocurrent being observed. As the photo illumination-induced desorption of gas molecules weakens for longer wavelengths, the bolometric effect dominates, and only positive photocurrent was observed for infrared light. Notably, the conductivity of thick $PdSe_2$ films is insensitive to gas molecular adsorption/desorption effects, and thus no NPC effect was observed for light in the UV to NIR. Although the co-existence of NPC and positive photoconductance (PPC) has been previously reported in graphene,[44] semiconducting Te,[47] and multilayer InSe,[48] the bolometric effect and surface-absorption-related NPC effect were first observed in 2D $PdSe_2$ material.

To gain a deeper understanding of the bolometric effect, the relative resistance changes with temperature were measured for $PdSe_2$ films with varying thicknesses, as shown in **Figure 5**a. The results demonstrate that the resistance decreases as the

temperature increases for all samples, indicating the semiconducting nature of the $PdSe_2$ films. Notably, the thinnest film exhibits the highest sensitivity to temperature, as evidenced by its more considerable relative resistance change compared to the thicker films. The measured data can be well fitted by the equation:

$$R = R_0 \exp\left(\frac{E_A}{k_B T}\right) \tag{3}$$

where R_0 is the resistance at $T \to \infty$, E_A is the activation energy, k_B is Boltzmann's constant, and T is the temperature. Thus, the $\ln(R)$ linearly depends on $1/T$ (Figure 5b). If the semiconductor is an intrinsic semiconductor, E_A is half of the band gap (E_g). Supposing $PdSe_2$ used here is an intrinsic semiconductor, the band gap can be estimated from Figure 5b and is shown in Figure 5c. The calculated band gap decreases with the increase of film thickness, consistent with that reported in the literature.[36,49] The infrared reflectance spectra of the films were also measured to determine the band gap of the $PdSe_2$ films (Figure S5, Supporting Information). The optical band gap determined from the spectra is also shown in Figure 5c. Though the exact value of the band gap determined for electric measurements and optical spectra is different, the variation trend with film thickness is the same. The results suggest that the main mechanism for the changes of resistance with temperature can be attributed to thermally generated electron holes across the band gap. Due to the small band gap of $PdSe_2$ and the detection wavelength limit of the spectrometer, absorbance data close to the band gap could not be obtained. Consequently, an extrapolation method was employed, as reported in the literature,[35] to determine the band gap. However, it should be noted that this method may result in a significant deviation from the actual band gap value. Moreover, the electronic band gap was determined assuming that the $PdSe_2$ films were intrinsic semiconductors, although they may deviate from this ideal, leading to smaller band gaps. Therefore, the difference between the optical and electronic band gaps can be attributed to the combined effect of these two factors. For the bolometric effect, the TCR is the most important parameter, which can be determined from the equation:

$$\mathrm{TCR} = \frac{1}{R}\frac{\mathrm{d}R}{\mathrm{d}T} = -\frac{E_g}{2k_B T^2} \tag{4}$$

The TCRs of the films at 30 °C were calculated according to the equation and are shown in Figure 5c. Clearly, the absolute value of TCR decreases with the increase in thickness.

We obtained the largest TCR to be −4.3% $°C^{-1}$ for the thinnest one, which is larger than that of metals,[50–53] most of the 2D materials,[12,54–57] amorphous Si,[58] and even commercial VO_x.[59,60] as can be seen in Figure 5d. To check the stability of the temperature-sensitive resistance, resistance-time curves at different temperatures were measured and are shown in Figure 5e. The observed resistance remains highly stable over time, as minimal or negligible changes are evident, thus suggesting a high level of resistance stability. Moreover, the low level of current noise renders the resistance easily distinguishable, even with a minute temperature variation of 0.1 °C. As the device is made on a PI substrate, it can be used in flexible devices. To check the stability of the device under repeated bending, the temperature-dependent resistances were measured after bending, as shown in Figure 5f. The near-coincidence of the curves suggests a high degree of stability for the flexible device, even after undergoing 500 bending cycles with a radius of 10 mm.

Due to the large TCR of the $PdSe_2$ films, the $PdSe_2$ photodetectors, also known as bolometers, can be used to collect infrared images. To demonstrate this capability, we constructed a 4 × 4 array of $PdSe_2$ bolometers capable of capturing infrared images. The imaging system schematic is presented in **Figure 6**a, where an IR lamp is illuminated on a shadow mask, and the device is placed beneath the mask to capture light signals. The letters in the mask can be reproduced from the recorded currents in the array, such as "UFO" shown in the figure. Moreover, the bolometric effect can not only be utilized in infrared photodetectors but also in thermal sensors. Figure 6b shows that the measured signal is highly sensitive to the distance between the device and the finger. The signal strength increases as the finger moves closer to the device, indicating its potential application as a thermal sensor. As an additional demonstration, a 4 × 4 array can record the temperature change of a "U" shaped hot object (Figure S6, Supporting information). The low thermal capacity resulting from the ultrathin nature of the films, combined with large TCR, makes the $PdSe_2$ film highly promising for ultrafast and highly sensitive thermal infrared detection. Incorporating proper device structural designs, such as adding a light absorption and/or reflection layer to enhance light absorption and using a bridged structure to further lower the thermal conductivity, can further improve the detection performance of the $PdSe_2$ films.

3. Conclusion

In summary, we have successfully realized broadband photodetectors using plasma-enhanced metal-selenization synthesized $PdSe_2$ films as the photosensitive material. The thick $PdSe_2$ film-based photodetectors exhibited decent performance, including high responsivity and fast response speed, while thin film-based devices (4.5-13 nm) showed both negative and positive photoresponses. We found that the bolometric effect dominated the photoresponse for the thicker film across all wavelength regions, whereas for the thinner film, it dominated the infrared region. The gas adsorption/desorption effect was identified as the cause of the NPC effect in the UV to VIS region of thinner $PdSe_2$ films. Detailed studies showed that the TCR value was closely related to film thickness, with the thinnest film having the largest absolute TCR value of up to 4.3% $°C^{-1}$. The value is more significant than that of metals, most 2D materials, amorphous Si, and even commercial VO_x. Moreover, we demonstrated the potential application of $PdSe_2$ in infrared imaging by utilizing a 4 × 4 photodetector array to record an infrared image. These findings suggest that $PdSe_2$ films hold great applications prospect in broadband photodetectors.

4. Experimental Section

$PdSe_2$ Film Preparation: Both PI and SiO_2/Si were used as substrates for the deposition of Pd films. Pd films (2–10 nm) were deposited in a direct current magnetron sputtering system. The selenization of the Pd

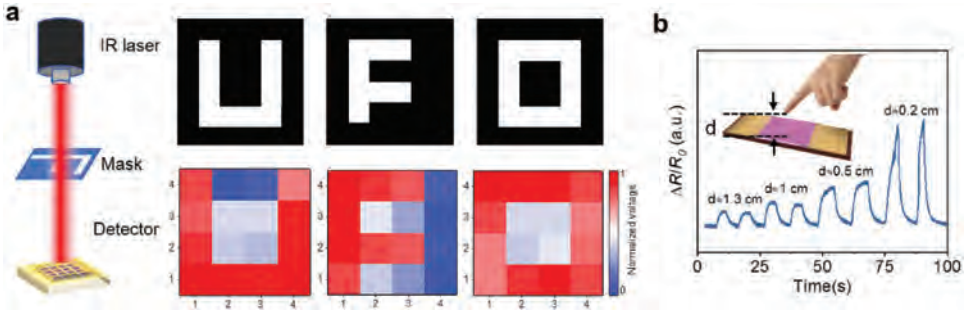

Figure 6. Infrared imaging and heat radiation measurement demonstrations. a) Schematic for detecting a shadow mask under irradiation with an IR fiber laser with a wavelength of 808 nm and the corresponding measured results. b) Relative change of resistance versus time as a human finger approaches the device at different distances.

films was carried out in a homemade remote plasma-enhanced CVD system with a horizontal tube furnace (OTF-1200X-S, HF-Kejing) and a radio frequency (RF) power generator (13.56 MHz, Beijing GMPOWER, 500 W). The Pd films were placed downstream, and Se powder (99.9%, 1 g) was placed upstream in the tube furnace. Before selenization, the pressure of the tube was pumped down to 1 Pa. Then 5 sccm Ar gas was introduced into the tube. During the selenization, the pressure inside the tube was maintained at 9 Pa. The typical selenization temperature and time are 200 °C and 30 min, respectively. Note that although Se powder is difficult to evaporate at 200 °C, the bombardment of Ar plasma can ionize Se atoms into Se radicals with higher chemical reactivity and then react with Pd atoms.

Film Characterization: The Raman spectrometer (Renishaw 1000) with an excitation wavelength of 532 nm was used to collect Raman signals of the films. The excitation power of the laser is ≈1 mW, and the spot size of the light is ≈2 µm. The XPS spectrometer (Axis Supra) with an Al K_α 300 W working source was used to collect the XPS signals of the films. HRTEM images were obtained by a field-emission transmission electron microscope (Thermo Fisher Scientific, Talos) operating at 200 kV. The cross-section of the films was prepared by using a focused ion beam system (Tescan GAIA 3). The film thickness and surface roughness were measured by an atomic force microscope (FM-Nanoview 1000). The absorbance of the film was measured by the UV–vis spectrophotometer (Shimadzu 3600iplus).

Device Fabrication and Measurement: To prepare the two-terminal devices, In/Au (8/50 nm) was deposited as an Ohmic contact to the $PdSe_2$ film by thermal evaporation. A fine Ag wire with a diameter of 30 µm was used as a shadow mask. Photoelectrical characterization of devices was carried out on a semiconductor parameter analyzer (4200A-CSC, Keithley Instruments) with light sources including light emitting diode (365 nm and 660 nm) and laser diodes (405, 532, 1550, and 2200 nm) in a vacuum probe station. The light intensity of the light sources was measured by a power meter (PM320E, Thorlabs). The temperature-dependent electrical properties of the device were measured on a thermal stage (SINO AGG, IST-600E). The TCR was determined using a two-probe *R*--*T* measurement from 30 to 80°C. A semiconductor analyzer (Keysight B1500A) with a variable temperature probe station (PicoFemto) was utilized to measure the electrical properties of the device under a temperature variation of 0.1 °C. The 4 × 4 device array was fabricated by a photolithography technique and illuminated by a fiber laser with a wavelength of 808 nm. The silver conducting epoxy was utilized for wiring these devices for imaging measurements. A Keithley 2400 resource meter and a Keithley 3723 relay multiplex card programmed by LabVIEW software were used to record the bias voltage signals of the resistor connected in series to the device array.

Supporting Information

Supporting Information is available from the Wiley Online Library or from the author.

Acknowledgements

This work was supported by the National Key Research and Development Program of China (Grant No. 2019YFB2203504), the National Natural Science Foundation of China (Grant Nos. 61975024 and 62074024), the Natural Science Foundation of Sichuan Province (Grant No. 2022NSFSC0042), and the Sichuan Science and Technology Program (Grant Nos. 2023YFH0090 and 2023NSFSC0365).

Conflict of Interest

The authors declare no conflict of interest.

Data Availability Statement

The data that support the findings of this study are available from the corresponding author upon reasonable request.

Keywords

palladium diselenides, photodetectors, temperature coefficient of resistances

Received: May 5, 2023
Revised: June 14, 2023
Published online: July 3, 2023

[1] M. Long, P. Wang, H. Fang, W. Hu, *Adv. Funct. Mater.* **2018**, *29*, 1803807.
[2] N. Huo, G. Konstantatos, *Adv. Mater.* **2018**, *30*, 1801164.
[3] Z. Zhao, C. Xu, L. Niu, X. Zhang, F. Zhang, *Laser Photonics Rev.* **2020**, *14*, 2000262.
[4] Q. Qiu, Z. Huang, *Adv. Mater.* **2021**, *33*, 2008126.
[5] J. Zha, M. Luo, M. Ye, T. Ahmed, X. Yu, D. H. Lien, Q. He, D. Lei, J. C. Ho, J. Bullock, K. B. Crozier, C. Tan, *Adv. Funct. Mater.* **2021**, *32*, 2111970.
[6] P. Avouris, C. Dimitrakopoulos, *Mater. Today* **2012**, *15*, 86.
[7] O. Lopez-Sanchez, D. Lembke, M. Kayci, A. Radenovic, A. Kis, *Nat. Nanotechnol.* **2013**, *8*, 497.
[8] Q. H. Wang, K. Kalantar-Zadeh, A. Kis, J. N. Coleman, M. S. Strano, *Nat. Nanotechnol.* **2012**, *7*, 699.
[9] H. O. Churchill, P. Jarillo-Herrero, *Nat. Nanotechnol.* **2014**, *9*, 330.

[10] M. R. Lien, N. Wang, J. Wu, A. Soibel, S. D. Gunapala, H. Wang, M. L. Povinelli, *Nano Lett.* **2022**, *22*, 8704.
[11] J. Wu, H. Yuan, M. Meng, C. Chen, Y. Sun, Z. Chen, W. Dang, C. Tan, Y. Liu, J. Yin, Y. Zhou, S. Huang, H. Q. Xu, Y. Cui, H. Y. Hwang, Z. Liu, Y. Chen, B. Yan, H. Peng, *Nat. Nanotechnol.* **2017**, *12*, 530.
[12] H. Yang, C. Tan, C. Deng, R. Zhang, X. Zheng, X. Zhang, Y. Hu, X. Guo, G. Wang, T. Jiang, Y. Zhang, G. Peng, H. Peng, X. Zhang, S. Qin, *Small* **2019**, *15*, 1904482.
[13] Y. Wang, L. Li, W. Yao, S. Song, J. T. Sun, J. Pan, X. Ren, C. Li, E. Okunishi, Y. Q. Wang, E. Wang, Y. Shao, Y. Y. Zhang, H. T. Yang, E. F. Schwier, H. Iwasawa, K. Shimada, M. Taniguchi, Z. Cheng, S. Zhou, S. Du, S. J. Pennycook, S. T. Pantelides, H. J. Gao, *Nano Lett.* **2015**, *15*, 4013.
[14] C. Yim, N. McEvoy, S. Riazimehr, D. S. Schneider, F. Gity, S. Monaghan, P. K. Hurley, M. C. Lemme, G. S. Duesberg, *Nano Lett.* **2018**, *18*, 1794.
[15] X. Yu, P. Yu, D. Wu, B. Singh, Q. Zeng, H. Lin, W. Zhou, J. Lin, K. Suenaga, Z. Liu, Q. J. Wang, *Nat. Commun.* **2018**, *9*, 1545.
[16] L. Zeng, D. Wu, J. Jie, X. Ren, X. Hu, S. P. Lau, Y. Chai, Y. H. Tsang, *Adv. Mater.* **2020**, *32*, 2004412.
[17] W. Yu, Z. Dong, H. Mu, G. Ren, X. He, X. Li, S. Lin, K. Zhang, Q. Bao, S. Mokkapati, *ACS Nano* **2022**, *16*, 12922.
[18] W. L. Chow, P. Yu, F. Liu, J. Hong, X. Wang, Q. Zeng, C. H. Hsu, C. Zhu, J. Zhou, X. Wang, J. Xia, J. Yan, Y. Chen, D. Wu, T. Yu, Z. Shen, H. Lin, C. Jin, B. K. Tay, Z. Liu, *Adv. Mater.* **2017**, *29*, 1602969.
[19] Q. Liang, Q. Wang, Q. Zhang, J. Wei, S. X. Lim, R. Zhu, J. Hu, W. Wei, C. Lee, C. Sow, W. Zhang, A. T. S. Wee, *Adv. Mater.* **2019**, *31*, 1807609.
[20] A. M. Afzal, G. Dastgeer, M. Z. Iqbal, P. Gautam, M. M. Faisal, *ACS Appl. Mater. Interfaces* **2020**, *12*, 19625.
[21] L. Pi, C. Hu, W. Shen, L. Li, P. Luo, X. Hu, P. Chen, D. Li, Z. Li, X. Zhou, T. Zhai, *Adv. Funct. Mater.* **2020**, *31*, 2006774.
[22] J. Wu, H. Ma, C. Zhong, M. Wei, C. Sun, Y. Ye, Y. Xu, B. Tang, Y. Luo, B. Sun, J. Jian, H. Dai, H. Lin, L. Li, *Nano Lett.* **2022**, *22*, 6816.
[23] Q. Liang, Z. Chen, Q. Zhang, A. T. S. Wee, *Adv. Funct. Mater.* **2022**, *32*, 2203555.
[24] G. Li, S. Yin, C. Tan, L. Chen, M. Yu, L. Li, F. Yan, *Adv. Funct. Mater.* **2021**, *31*, 2104787.
[25] M. Long, Y. Wang, P. Wang, X. Zhou, H. Xia, C. Luo, S. Huang, G. Zhang, H. Yan, Z. Fan, X. Wu, X. Chen, W. Lu, W. Hu, *ACS Nano* **2019**, *13*, 2511.
[26] J. Yu, X. Kuang, J. Li, J. Zhong, C. Zeng, L. Cao, Z. Liu, Z. Zeng, Z. Luo, T. He, A. Pan, Y. Liu, *Nat. Commun.* **2021**, *12*, 1083.
[27] Z. Dong, W. Yu, L. Zhang, H. Mu, L. Xie, J. Li, Y. Zhang, L. Huang, X. He, L. Wang, S. Lin, K. Zhang, *ACS Nano* **2021**, *15*, 20403.
[28] L.-B. Luo, D. Wang, C. Xie, J.-G. Hu, X.-Y. Zhao, F.-X. Liang, *Adv. Funct. Mater.* **2019**, *29*, 1900849.
[29] L. H. Zeng, Q. M. Chen, Z. X. Zhang, D. Wu, H. Yuan, Y. Y. Li, W. Qarony, S. P. Lau, L. B. Luo, Y. H. Tsang, *Adv. Sci.* **2019**, *6*, 1901134.
[30] A. M. Afzal, M. Z. Iqbal, G. Dastgeer, A. u. Ahmad, B. Park, *Adv. Sci.* **2021**, *8*, 2003713.
[31] D. Wu, C. Jia, F. Shi, L. Zeng, P. Lin, L. Dong, Z. Shi, Y. Tian, X. Li, J. Jie, *J. Mater. Chem. A* **2020**, *8*, 3632.
[32] A. M. Afzal, M. Z. Iqbal, S. Mumtaz, I. Akhtar, *J. Mater. Chem. C* **2020**, *8*, 4743.
[33] F. X. Liang, X. Y. Zhao, J. J. Jiang, J. G. Hu, W. Q. Xie, J. Lv, Z. X. Zhang, D. Wu, L. B. Luo, *Small* **2019**, *15*, 1903831.
[34] X. Kang, C. Lan, F. Li, W. Wang, S. Yip, Y. Meng, F. Wang, Z. Lai, C. Liu, J. C. Ho, *Adv. Opt. Mater.* **2021**, *9*, 2001991.
[35] L.-H. Zeng, D. Wu, S.-H. Lin, C. Xie, H.-Y. Yuan, W. Lu, S. P. Lau, Y. Chai, L.-B. Luo, Z.-J. Li, Y. H. Tsang, *Adv. Funct. Mater.* **2019**, *29*, 1806878.
[36] A. D. Oyedele, S. Yang, L. Liang, A. A. Puretzky, K. Wang, J. Zhang, P. Yu, P. R. Pudasaini, A. W. Ghosh, Z. Liu, C. M. Rouleau, B. G. Sumpter, M. F. Chisholm, W. Zhou, P. D. Rack, D. B. Geohegan, K. Xiao, *J. Am. Chem. Soc.* **2017**, *139*, 14090.
[37] S. Jiang, C. Xie, Y. Gu, Q. Zhang, X. Wu, Y. Sun, W. Li, Y. Shi, L. Zhao, S. Pan, P. Yang, Y. Huan, D. Xie, Q. Zhang, X. Liu, X. Zou, L. Gu, Y. Zhang, *Small* **2019**, *15*, 1902789.
[38] X. Chen, J. Huang, C. Chen, M. Chen, G. Hu, H. Wang, N. Dong, J. Wang, *Adv. Opt. Mater.* **2021**, *10*, 2101963.
[39] Y. Zhang, X. Wang, Y. Zhou, H. Lai, P. Liu, H. Chen, X. Wang, W. Xie, *Nano Lett.* **2022**, *1*, 485.
[40] F. H. Koppens, T. Mueller, P. Avouris, A. C. Ferrari, M. S. Vitiello, M. Polini, *Nat. Nanotechnol.* **2014**, *9*, 780.
[41] V. J. Gokhale, M. Rais-Zadeh, *J. Microelectromech. S.* **2014**, *23*, 803.
[42] S. Anderson, L. Dzhavadovt, *J. Phys.: Condens. Matter* **1992**, *4*, 6209.
[43] S. Wei, Q. Yu, Z. Fan, S. Liu, Z. Chi, X. Chen, Y. Zhang, J. Xu, *RSC Adv.* **2018**, *8*, 22169.
[44] C. Biswas, F. Gunes, D. L. Duong, S. C. Lim, M. S. Jeong, D. Pribat, Y. H. Lee, *Nano Lett.* **2011**, *11*, 4682.
[45] A. Grillo, E. Faella, A. Pelella, F. Giubileo, L. Ansari, F. Gity, P. K. Hurley, N. McEvoy, A. Di Bartolomeo, *Adv. Funct. Mater.* **2021**, *31*, 2105722.
[46] A. Di Bartolomeo, A. Pelella, X. Liu, F. Miao, M. Passacantando, F. Giubileo, A. Grillo, L. Iemmo, F. Urban, S. J. Liang, *Adv. Funct. Mater.* **2019**, *29*, 1902483.
[47] R. Wang, J. L. Wang, T. Liu, Z. He, H. Wang, J. W. Liu, S. H. Yu, *Adv. Mater.* **2022**, *34*, 2204698.
[48] Y. Wang, J. Gao, B. Wei, Y. Han, C. Wang, Y. Gao, H. Liu, L. Han, Y. Zhang, *Nanoscale* **2020**, *12*, 18356.
[49] M. Wei, J. Lian, Y. Zhang, C. Wang, Y. Wang, Z. Xu, *npj 2D Mater. Appl.* **2022**, *6*, 1.
[50] W. F. Leonard, R. L. Ramey, *J. Appl. Phys.* **1966**, *37*, 3634.
[51] R. B. Belser, W. H. Hicklin, *J. Appl. Phys.* **1959**, *30*, 313.
[52] S. M. Shivaprasad, M. A. Angadi, *J. Phys. D: Appl. Phys.* **1980**, *13*, L171.
[53] G. C. A. Kumar, O. P. Katyal, *J. Mater. Sci.* **1988**, *23*, 2361.
[54] J. S. Kim, J. Kim, J. Zhao, S. Kim, J. H. Lee, Y. Jin, H. Choi, B. H. Moon, J. J. Bae, Y. H. Lee, S. C. Lim, *ACS Nano* **2016**, *10*, 7500.
[55] A. I. Khan, P. Khakbaz, K. A. Brenner, K. K. H. Smithe, M. J. Mleczko, D. Esseni, E. Pop, *Appl. Phys. Lett.* **2020**, *116*, 203105.
[56] W. Ma, Y. Gao, L. Shang, W. Zhou, N. Yao, L. Jiang, Q. Qiu, J. Li, Y. Shi, Z. Hu, Z. Huang, *Adv. Sci.* **2022**, *9*, 2103873.
[57] H. Van Bui, A. Y. Kovalgin, J. Schmitz, R. A. M. Wolters, *Appl. Phys. Lett.* **2013**, *103*, 051904.
[58] B. F. Andresen, E. Mottin, G. F. Fulop, J.-L. Martin, J.-L. Ouvrier-Buffet, M. Strojnik, M. Vilain, A. Bain, J.-J. Yon, J.-L. Tissot, J.-P. Chatard, presented at*Infrared Technology and Applications XXVII*, Orlando, FL, USA, **2001**.
[59] A. Subrahmanyam, Y. Bharat Kumar Redd, C. L. Nagendra, *J. Phys. D: Appl. Phys.* **2008**, *41*, 195108.
[60] M. Gurvitch, S. Luryi, A. Polyakov, A. Shabalov, *J. Appl. Phys.* **2009**, *106*, 104504.